

Tuning magnetic response of epitaxial iron-silicide nanoislands by controlled self-assembled growth

I. Goldfarb,^{*} Y. Camus, M. Dascalu, F. Cesura, R. Chalasani, and A. Kohn*Department of Materials Science and Engineering, Faculty of Engineering, Tel Aviv University, Ramat Aviv, Tel Aviv 6997801, Israel*

(Received 2 March 2017; revised manuscript received 15 June 2017; published 13 July 2017)

We investigated the dependence of the magnetic response from epitaxial Si-rich iron-silicide nanostructures on their geometry. By varying substrate orientation and deposition parameters, we altered the growth kinetics and the lattice matching conditions at the silicide/silicon interface. These affected the silicide nanoisland crystal structure, size, shape, and proximity due to spatial ordering and, consequently, their magnetic response in terms of shape and opening of the respective hysteresis loops. In particular, we demonstrated correlation between magnetic anisotropy, expressed as the hysteresis coercive field, and the nanoisland spatial length-to-width aspect ratio. This correlation is explained by the contribution of undercoordinated island edge atoms to the overall measured magnetic behavior of the nanoisland arrays. Further, the island self-ordering along periodic surface steps adds dipolar interactions between the otherwise superparamagnetic nanoislands, consequently resulting in a magnetic response resembling that of a superspin glass.

DOI: [10.1103/PhysRevB.96.045415](https://doi.org/10.1103/PhysRevB.96.045415)

I. INTRODUCTION

The interest in epitaxial/self-assembled (SA) (bottom-up) or lithographically defined (top-down) magnetic nanostructures (MNSs) is due to fundamental mesoscopic and nanoscale physics and their technological potential for spin electronics [1–10]. Ferromagnets exhibit both temperature-dependent and size-dependent transitions. Ferromagnets turn paramagnetic above the Curie temperature (T_C) and can exhibit a superparamagnetic (SPM) state below a critical single domain size. Therefore, SPM often takes place in nanostructures, where, at least in the static regime, multidomain micromagnetic structures become energetically unfavorable, facilitating ensembles of noninteracting single-domain nanoparticles instead [5,11,12]. The SPM state shows paramagneticlike S-shape closed magnetization curves with high magnetic susceptibility above a blocking temperature ($T_b < T_C$) and a hysteresis loop below T_b because reversal of magnetic moments is slower than the measurement time. Size-dependent magnetic properties and response of the MNS make them a scientifically and technologically attractive new class of materials [13–15]. However, at these single-domain dimensions, typically a few tens of nanometers, the size-dependent T_b , where magnetic anisotropy energy (MAE) is comparable to the thermal energy, is often significantly below room temperature (RT) [1,11,16]. This phenomenon is the main obstacle to implementation of MNS as ultrahigh-density magnetic recording materials [17] and magneto-optically active nanocomposites [18]. These devices require easy-axis anisotropy with high remanence and large coercive fields, which for many MNSs occurs at temperatures below RT, too low for technological applications. Often times, the coercivity gradually increases with decreasing size down to a critical, single-domain size. Further reduction of the MNS below this size causes a sharp decrease in coercivity down to zero [19]. Therefore, the challenge for ultrahigh density data storage is to fabricate MNS with reduced size while delaying the onset of superparamagnetism [20]. This can be done by

finding materials or MNSs with high magnetic anisotropies [21] to yield correspondingly high coercivities [22,23].

While top-down lithography methods allow for precision and repeatability of the fabricated features, bottom-up SA and its higher degree in terms of positional ordering, named self-organization or self-ordering (SO), offer tailoring of the nanodeposit structural, morphological, and magnetic characteristics resolved to various stages of evolution [14,24–27]. A popular method of SA is heteroepitaxial growth, where the desired species are evaporated onto a well-defined surface in ultrahigh vacuum (UHV). These species form nanostructures by spontaneous nucleation and growth due to a combination of chemical, thermodynamic, and kinetic factors. Metal silicides readily SA on Si substrates, when metallic adatoms are supplied to the surface and heated to catalyze the metal-silicon (Me -Si) reaction, either during deposition [reactive deposition epitaxy (RDE)] or by postdeposition anneals [solid phase epitaxy (SPE)] [28–33]. By varying substrate orientation and hence the surface symmetry and periodicity, the geometric shape of the growing nanostructures can be controlled to some degree due to crystallographic constraints imposed by anisotropy and lattice match conditions. For example, while twofold symmetry of the {001} and {110} surfaces favors elongated shapes [34–36], nanostructures growing on a threefold symmetrical {111} surface attain a more compact, hexagonal shape [37]. Growth on periodically stepped vicinal surfaces provides more control over size and positioning of the nanostructures, which SO along the ledges by a step-decoration mechanism [38–41]. Finally, compatibility of silicide MNS with Si-based process engineering adds a technological incentive for their exploration.

Me_xSi_{1-x} MNS based on ferromagnetic transition metals (where $Me = Fe, Ni, Co$ and $x \geq 0.5$ as a minimal prerequisite for ferromagnetism) have been successfully realized [42–46] because most equilibrium binary Me -Si diagrams contain several Me -rich phases, typically Me_3Si , Me_2Si , and Me_5Si_3 . The Fe-Si system, for example, has Fe_3Si and Fe_5Si_3 , which attract interest for spintronic devices, especially the Heusler-type Fe_3Si [47,48]. Magnetic silicides can significantly simplify fabrication of nanomagnets because deposition of buffer layers for preventing ferromagnet-silicon reaction [49] may no longer be necessary. Surprisingly, even in silicide MNS with $x < 0.5$,

^{*} Also at: Research Center for Nanoscience and Nanotechnology, Tel Aviv University, Ramat Aviv, Israel; ilang@eng.tau.ac.il

such as FeSi_2 nanostructures, a ferromagnetic response has been reported [36,50–52], including by Tripathi *et al.* [40,41]. To date, this phenomenon has been explained mostly by local Fe-rich defects expected in nanostructures [50–53]. Such defects are likely to form at discontinuities of the crystal lattice, such as surfaces, interfaces, edges, and corners, where atoms are undercoordinated. In sufficiently small nanostructures, the relative proportion of such boundaries may prevail over the volume. Indeed, Rusponi *et al.* have shown that edge atoms in Co monolayer islands on Pt(111) contribute 20 times more MAE than the surface and bulk atoms altogether [54].

In view of the contribution of edge atoms, higher coercivities are expected in elongated structures, where perimeters dominate over surface areas. In this paper, we varied geometric shapes by epitaxially growing FeSi_2 nanoislands with different crystal structures. While FeSi_2 phases are paramagnetic in their bulk form, we demonstrate that edge atoms facilitate ferromagnetic ordering in epitaxial FeSi_2 . The increase of magnetic coercivity, acquired with the nanoisland mean length-to-width aspect ratio, indicates a significant contribution of edge atoms.

II. EXPERIMENTAL

Experiments were conducted in an UHV variable-temperature scanning tunneling microscope (VT-STM) by Omicron Nanotechnology GmbH, equipped with low- (LEED) and reflection high- (RHEED) energy electron diffraction (20 kV), Auger electron spectrometer (AES), and capable of operation up to 1250 °C by direct-current heating, as described in our recent works [30–33,37–41,55]. The 4°-miscut Si(111) and 2°-miscut Si(001) wafers were cut into 10 mm×1 mm strips, chemically degreased and cleaned *ex vacuo*. In UHV (base pressure 1×10^{-8} Pa), after thorough degassing, the oxide was evaporated by repeated flashes at 1150–1200 °C. The clean Si surface was then cooled slowly until both diffraction and STM showed well-ordered (7×7) and mixed (2×1) + (1×2) reconstructions in case of Si(111) and Si(001), respectively. Subsequently, Fe was e-beam evaporated from a pure wire onto the both substrate types held at RT. Consequently, the samples underwent annealing treatments under continuous STM imaging so that a particular evolving surface morphology could be fixed and the sample removed for *ex-situ* analyses. The initial Fe coverage, θ , was estimated from image analysis of unreacted metal clusters immediately after the deposition, assuming a spherical shape, as described elsewhere (cf. Refs. [37–41] and [55]). Thus, samples S1, S2, and S3 and samples S4 and S5 were obtained on Si(001) and Si(111) surfaces, respectively. For example, S1 and S3 were obtained by a single annealing step of a few and ~ 1 –2 equivalent monolayers (eq. MLs, where 1 eq. ML of Fe = 0.70×10^{15} atoms/cm²) by heating to 550 °C. Sample S2, with a sub-ML Fe coverage, was gradually annealed to 750 °C throughout several annealing cycles, with STM control inspection after each cycle in order to stop the experiment once the desired morphology appeared. Samples S4 and S5 were obtained in this mode, with a terminating annealing step at 500 °C and 550 °C, respectively, of different initial Fe coverages: $1 < \theta < 2$ eq. MLs in the S5 case, and higher coverage $2 < \theta < 10$ eq. MLs in the S4 case. None of the samples exceeded coverage of 10 MLs.

The STM images were acquired using tunneling conditions of $0.1 \text{ nA} < I < 0.2 \text{ nA}$ and $-3.0 \text{ V} < V < +3.0 \text{ V}$ in a constant-current mode and shown as current (I rather than z) images because in most cases I images are easier to visualize. Image processing and topographic measurements, though, were naturally conducted on the z images. The scanning was 45° rotated relative to the sample stripe sides for better imaging. While STM collects images in forward and backward scan directions, only images acquired in a forward direction are shown here. Freeware Image SXM by Steve Barrett and a commercial image processing SPIP software from Image Metrology were used for postacquisition STM image measurements and statistical analyses of the island dimensions and geometric shape distributions. The x-ray photoelectron spectroscopy (XPS) measurements were conducted *ex situ* in a UHV (3.0×10^{-8} Pa base pressure) 5600 multitechnique system (Philadelphia, Pennsylvania, USA) using a monochromated x-ray excitation source (Al K α : 1486.6 eV) and a spherical capacitor analyzer with a 0.8 mm slit aperture for the emitted photoelectron analysis. Magnetic measurements were conducted *ex situ* using a Quantum Design MPMS XL5 superconducting quantum interference device (SQUID) magnetometer in a vibrating sample magnetometer (VSM) mode. The magnetic field was applied parallel (as well as perpendicular) to the surface along Si (110) crystallographic directions in the both substrate orientations at temperatures of 4 K, 150 K, and 300 K. The diamagnetic background was subtracted after measuring an identical bare Si substrate at applied fields between 20 and 60 kOe. Field cooled (FC) measurements were undertaken at an applied field of 1 kOe.

Selected samples were prepared for cross-sectional observation by transmission electron microscopy (TEM) along the Si[110] zone axis and parallel to the surface steps. The TEM samples were prepared by mechanical polishing and low-energy Ar ion milling. High-resolution phase contrast (HR-TEM) and z -contrast high angle annular dark field (HAADF) scanning TEM (STEM) was applied using a JEOL JEM 2100F TEM.

III. RESULTS

A. Structural analysis on Si(001)

Typical island shapes on Si(001) and Si(111) are shown in Figs. 1(a)–1(d) and Figs. 1(e)–1(g), respectively. While the islands in all samples [Figs. 1(a)–1(f)] are SA, the large polyhedral islands in S5 [Figs. 1(f) and 1(g)] are additionally SO along the figure diagonal, forming 1D island chains decorating the Si(111) step-bunch edges, with the same interchain terrace-wide separation as the step-bunches on our vicinal Si(111) surface, and having the same in-plane (110) orientation as the step-bunches. This 1D SO is quite perfect and extends over many micrometers [Fig. 1(g)]. Such a high degree of SO requires a low initial Fe coverage (~ 1 –2 eq. MLs) followed by a slow postdeposition annealing up to 500–550 °C, as described in our previous publications (e.g., Ref. [40], which captures in detail all the stages of ordering, from disordered as-deposited Fe coverage to a perfectly ordered step decoration). A higher coverage of a few eq. MLs in S4, annealed up to 500 °C, resulted in a mixed surface with flat

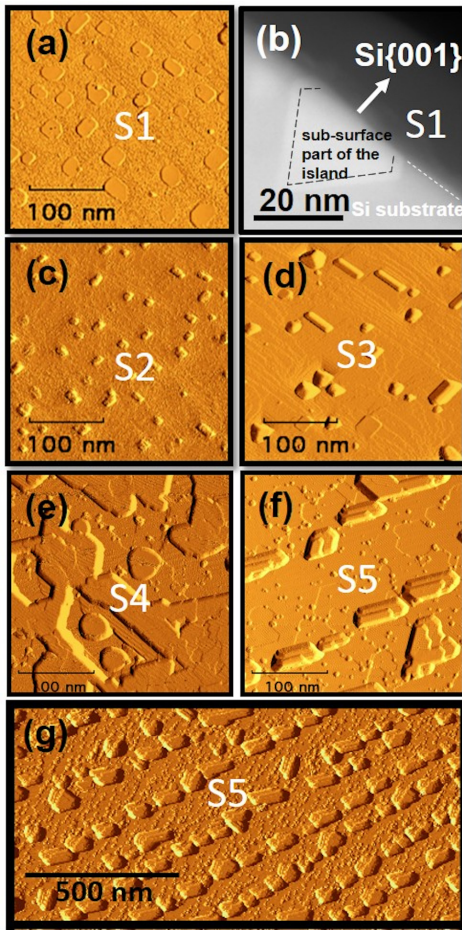


FIG. 1. Typical epitaxial iron-silicide nanostructures on Si surfaces. (a), (c), (d) Constant-current STM I images on Si(001) and (e)–(g) Si(111) substrates. (b) Cross-sectional z -contrast STEM micrograph (Si substrate oriented to the [110] zone axis) of a characteristic flat-top disklike island in S1 sample in (a). Step and island edge and elongation directions are parallel to $\langle 110 \rangle$ on both substrate orientations.

circular islands surrounded by quasicontinuous film shown in Fig. 1(e), resembling closely that described by Wawro *et al.*, including a strong electronic contribution to the STM contrast [56]. The flat-top S1 disks on Si(001) in Fig. 1(a), of about $1 \text{ nm} \pm 0.5 \text{ nm}$ height above the surface, show distinct subsurface facets in the cross-sectional z -contrast STEM image in Fig. 1(b). The S3 islands, seen in Fig. 1(d), are elongated huts of various lengths. Figure 1(c) shows S2 islands, which are slightly elongated bars, namely intermediate structures between the S1 and S3 shapes.

A wide variety of stable iron-silicide phases exist in the equilibrium Fe-Si phase diagram [57], namely cubic Heusler-type Fe_3Si , Fe_2Si , Fe_5Si_3 , cubic ε -FeSi, tetragonal α -FeSi₂, and orthorhombic β -FeSi₂. Many of these phases can coexist in thin films, as well as a number of metastable structures stabilized epitaxially on silicon (001) and (111) surfaces by good lattice match conditions. Most notable of these is the cubic CaF₂-type γ -FeSi₂ and CsCl-type defected Fe_{1-x}Si structure with $0 < x < 0.5$ [58–69]. The wide variety of possible phases complicates their unambiguous identification,

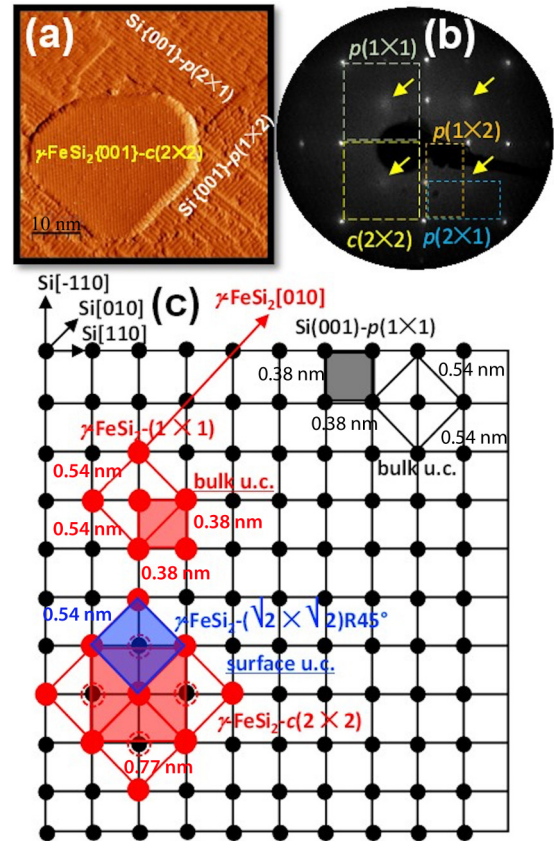


FIG. 2. (a) High-resolution STM I image of a characteristic flat-top disklike island from the S1 sample, as shown in Figs. 1(a), and 1(b) the corresponding 90 eV LEED pattern. Reciprocal lattice deduced from (b) well corroborates the real-space structure of the S1 surface in (a), including the three observed reconstructions marked in (a) and (b). (c) Ball-and-stick 2D schematic representation of the epitaxial orientation relations between the flat-top γ -FeSi₂ islands and the Si(001) substrate surface.

especially considering close similarity of crystal structures and lattice constants, at least along certain crystal faces. For example, Fe_3Si , α -FeSi₂, γ -FeSi₂, and CsCl- Fe_{1-x}Si can be derived from a face-centered (F) lattice with various and interchangeable occupancies of lattice sites and tetrahedral and octahedral interstices. This may explain conflicting reports on the silicide phases and structures found in epitaxial films [58–69] and on their evolution as a function of the initial coverage and annealing temperature [70–75]. The central goal of this paper was to distinguish between the relative bulk (e.g., crystal structure) and size (and shape) contributions to the measured magnetic properties. Therefore, all the relevant silicide structures found on our surfaces had to be identified.

Figure 2(a) shows a HR STM image of a compact flat-top island, characteristic of islands populating the surface of S1 depicted in Fig. 1(a). Lattice fringes, separated by 0.54 nm and rotated by 45° with respect to dimer rows of the Si(001)-(2×1) reconstructed surface between the islands are visible, forming a well-known $(\sqrt{2} \times \sqrt{2})\text{R}45^\circ$ aka $c(2 \times 2)$ reconstruction with respect to the Si(001)-(1×1) unit cell. The LEED pattern in Fig. 2(b) supports this determination: It showed intense base (×1) and superlattice half-order (×2) spots from the mixed

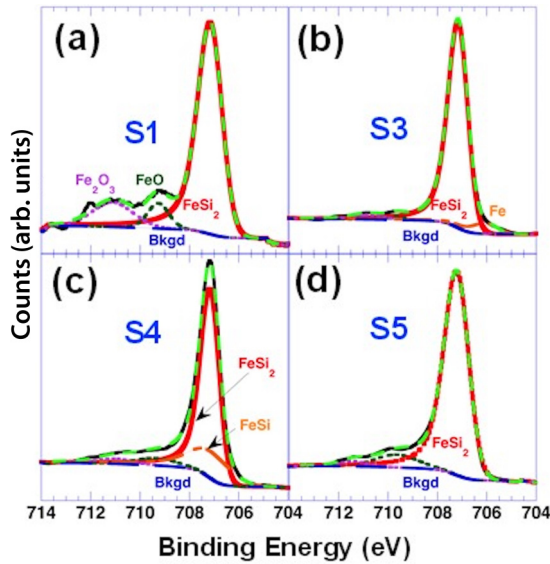


FIG. 3. High-resolution XPS Fe $2p_{3/2}$ core-level spectra of Fe-silicide samples (a) S1, (b) S3, (c) S4, and (d) S5. The background (thin continuous blue line, marked Bkgd) was subtracted using the Shirley method. Broken line describes the envelope intensity.

$(2 \times 1) + (1 \times 2)$ majority surface of bare Si and diffused $c(2 \times 2)$ spots (pointed to by yellow arrows) from the minority phase islands covering only part of the surface. As noted previously, judging solely from ~ 0.77 nm interatomic distances along $\langle 110 \rangle$ directions and fourfold symmetry of the $c(2 \times 2)$, this reconstruction can be attributed to cubic silicide phases (Fe_3Si , $\gamma\text{-FeSi}_2$, and $\text{CsCl-Fe}_{1-x}\text{Si}$), tetragonal $\alpha\text{-FeSi}_2$, and even (100) face of the orthorhombic $\beta\text{-FeSi}_2$. Indeed, identically reconstructed and similarly shaped Fe-silicide islands on Si(001) have been occasionally identified as $\beta\text{-FeSi}_2$ [58]. However, according to proposed growth phase diagrams, formation of $\beta\text{-FeSi}_2$ requires substantially thicker layers, with initial coverages well in excess of 10 eq. MLs of Fe [70–75], way beyond the coverage of samples S1–S5 in this paper. Formation of Fe_3Si was ruled out by XPS analysis of S1 and S3–S5, shown in Fig. 3. The S2 Fe photoelectron signal was too low to analyze. The Si $2p$ peak is hardly affected by the formation of silicides, and the Fe $2p_{3/2}$ peaks of the neighboring silicide valence states are too closely spaced for confident quantitative phase analysis. However, enhanced metallicity of the Fe-rich (and Ni-rich) silicides causes highly asymmetric tails on the high binding energy (BE) side of the Fe $2p_{3/2}$ peak, which is better fitted with a Doniach-Sunjc (DS) function. This was not the case with the Fe-silicide samples here, which exhibit rather symmetric Fe $2p_{3/2}$ peaks that could not be well fitted with a DS function (thick continuous red line). In our case the asymmetry parameters were in the $0.01 < \alpha < 0.08$ range, namely an order of magnitude lower than those extracted from Fe-rich silicides [76–78], e.g., $0.17 < \alpha < 0.40$ [76]. The unusually high asymmetry of S1 in Fig. 3(a) is attributed to excessive oxidation due to a prolonged exposure to the ambient atmosphere, so better fitted with FeO and Fe_2O_3 Gaussian-Lorentzian (GL) peak shapes [Fig. 3(a)].

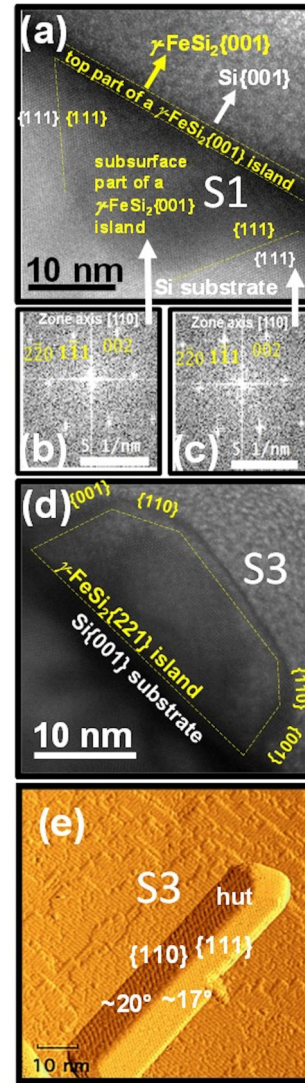


FIG. 4. The HR-TEM (phase contrast) cross-sectional images of the (a) flat-top S1 and (d) hut-shaped S3 [*I*-image STM magnified in (e)] iron-silicide islands from Figs. 1 and 2. (b), (c) Power spectra from lattice fringes of the submerged part of the island and of the substrate, respectively. The power spectrum of the hut in (d) was identical (not shown).

Cross-sectional z -contrast STEM analysis in Fig. 1(b) revealed symmetrical facets at an angle of $\sim 55^\circ$ with respect to the Si(001) surface. The crystal structure of the silicide islands is of a CaF_2 prototype, as determined from the reflections in the power spectra of HR-TEM images [cf. Fig. 4(b)]. These images were recorded from the subsurface portions of the islands [see Fig. 4(a)]. The power spectra in Figs. 4(b) and 4(c) also show, within the accuracy of TEM measurements, that the lattice constant of the CaF_2 -based structure is indistinguishable from that of Si (0.543 nm).

Thus, only one silicide structure matches the STM, LEED, XPS, and TEM results and lies within the < 10 eq. MLs temperature-coverage region in the proposed growth phase diagrams [70–75], namely the metastable $\text{CaF}_2\gamma\text{-FeSi}_2$ with orientation relations to Si{001} shown in Fig. 2(c). Moreover,

Ong *et al.* [79] reported for CaF_2 CoSi_2 on $\text{Si}\{001\}$ this type of flat-top island, with $\{001\} \parallel \text{Si}\{001\}$ and $\{111\}$ facets on the $\text{Si}\{111\}$ planes. Furthermore, long facets of the hut-shaped islands in sample S3, shown in Fig. 1(d) and magnified in Fig. 4(e), formed $\sim 20^\circ$ and $\sim 17^\circ$ ($\pm 1.5^\circ$) angles with the $\{221\}$ plane $\parallel \text{Si}\{001\}$ surface (as measured from STM height profile plots across numerous islands after using a line-by-line linear combined with a three-point compensation algorithm), corresponding to $\{111\}$ and $\{110\}$ CaF_2 planes. The island shapes were comparable to the fluorite CoSi_2 huts on $\text{Si}\{001\}$ grown by Ong *et al.* [79] and by the authors [32,34] (with flat CaF_2 $\gamma\text{-FeSi}_2\{221\} \parallel \text{Si}\{001\}$ interface in our case) and exhibited fluorite lattice image and Fourier power spectrum identical to those from the subsurface portion of the flat-top islands [see Fig. 4(e)]. The short faces at the hut edges were identified as $\{001\}$ and $\{110\}$. The mean hut height and standard deviation of the mean were measured by SPIP software to be $2.0 \text{ nm} \pm 0.7 \text{ nm}$. The islands in sample S2 had flat tops like the S1 islands, yet were taller and narrower, more like the islands in S3, thus an intermediate of the two shapes. These islands emerged from the lowest, submonolayer Fe coverage and appeared featureless even at HR STM imaging.

B. Structural analysis on vicinal $\text{Si}\{111\}$

Evolution of the Fe-covered vicinal $\text{Si}\{111\}$ surfaces proceeded according to our terrace ledge kink (TLK)-based model for silicide growth on stepped surfaces [38–40], in agreement with other reports [56,80]. At coverages of 1–2 eq. MLs, the SO of 3D iron-silicide islands along the step-bunch edges is possible [56,80], as in sample S5 shown in Fig. 1(f), because the adatom mean free path is comparable with the terrace width. At higher coverages, the probability of island formation in the midst of terraces increases [38–40,56–80], as in sample S4 shown in Figs. 1(e) and 5. Figure 5 shows HR STM I images of the complex S4 surface, and Fig. 6 demonstrates our z -image STM analysis of the surface symmetry and periodicity for the two prevailing surface structures, identifying them as $p(2 \times 2)$ and $(\sqrt{3} \times \sqrt{3})R30^\circ$, respectively. Due to the above mentioned crystallographic similarity between the majority of possible Fe-silicide structures found in the equilibrium phase diagram and in thin epitaxial deposits, the $p(2 \times 2)$ on top of the quasicontinuous layer in Fig. 5 could terminate most of them [56–78,80]. However, our less than 10 eq. ML coverage narrows the selection to CaF_2 ($\gamma\text{-FeSi}_2$), CsCl (Fe_{1-x}Si), or both: Most growth diagrams show that these two metastables can coexist in the coverage-temperature ranges typical of our experiments [70–75]. Nevertheless, since we found no evidence of $\text{CsCl-Fe}_{1-x}\text{Si}$ under similar experimental conditions on $\text{Si}\{001\}$, $\gamma\text{-FeSi}_2$ seems a more likely candidate.

The most plausible candidate for the isolated $(\sqrt{3} \times \sqrt{3})R30^\circ$ -reconstructed circular islands surrounded by the $p(2 \times 2)$ -reconstructed layer, on the other hand, is cubic $\varepsilon\text{-FeSi}$ [59,65,66,81–83]. This stable monosilicide phase has a lattice constant of $\sim 0.45 \text{ nm}$ (cf. Refs. [61], [63], and [64]), i.e., significantly smaller than that of other silicide structures derived from the face-centered cell, with lattice constants much closer to that of Si ($\sim 0.35 \text{ nm}$). This can explain the highly strained ($>4\%$) silicide $\{111\} \parallel \text{Si}\{111\}$ and $\langle 110 \rangle$ (i.e.,

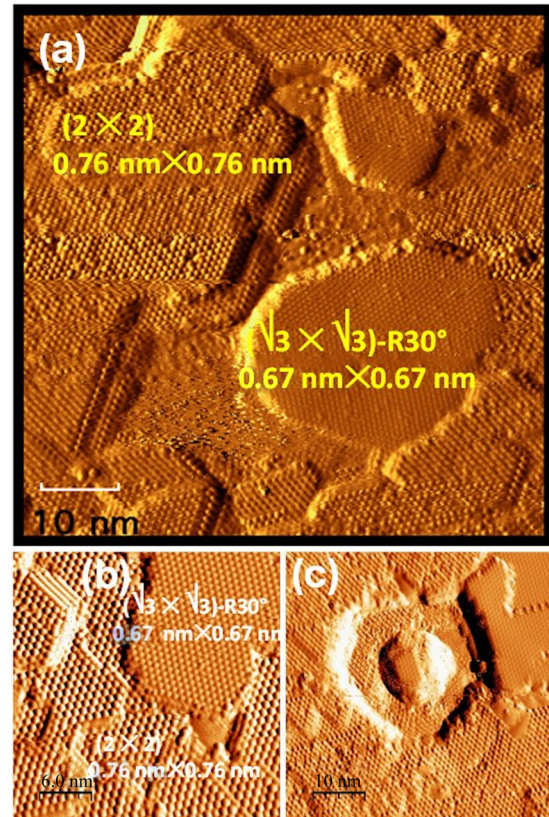


FIG. 5. (a) High-resolution I -image STM of the S4 sample surface, showing mixed (2×2) and $(\sqrt{3} \times \sqrt{3})R30^\circ$ structures, with occasional (b) thickening and (c) ripening of the $(\sqrt{3} \times \sqrt{3})R30^\circ$ islands.

$\sim 0.63 \text{ nm}$) $\parallel \text{Si}\langle 112 \rangle$ (i.e., $\sim 0.66 \text{ nm}$) orientation relations leading to a $(\sqrt{3} \times \sqrt{3})R30^\circ$, as in Figs. 5 and 6. Despite this high strain, these relations represent the best possible match between $\varepsilon\text{-FeSi}$ and $\text{Si}\{111\}$. Contrary to that, the best match and lowest strain orientation relations between Si and $\gamma\text{-FeSi}_2$, $\text{CsCl-Fe}_{1-x}\text{Si}$, and even tetragonally distorted $\alpha\text{-FeSi}_2$ are the simplest cube-on-cube ones. On a $\text{Si}\{111\}$ surface, that means silicide $\{111\} \parallel \text{Si}\{111\}$ and $\langle 110 \rangle \parallel \text{Si}\langle 110 \rangle$, leading to a well-known $p(2 \times 2)$ reconstruction with 0.76 nm lattice constant corresponding to double interatomic Si distances along $\langle 110 \rangle$ direction. Indeed, this low-energy reconstruction was observed on the $\gamma\text{-FeSi}_2$ film covering the S4 sample surface [Figs. 1(e), 5, and 6], as well as on the $\alpha\text{-FeSi}_2$ 3D islands (confirmed by TEM analysis in Ref. [40]) in S5 [Figs. 1(f) and 7(b)]. The difference in strain energy was manifested by the relative proportion of the two in S4. Most of the S4 surface was covered by the low-energy $p(2 \times 2)$ $\gamma\text{-FeSi}_2$ film, speckled with only several small $(\sqrt{3} \times \sqrt{3})R30^\circ$ islands, though locally those islands could thicken [Fig. 5(b)] and even ripen to a 3D dome shape by consuming the surrounding film and leaving circular denuded zones around them [Fig. 5(c)].

C. Magnetic measurements

Figures 7(a)–7(c) show magnified STM images of the characteristic silicide island shapes of samples S1–S3, respectively. Figures 7(d)–7(f) show their corresponding normalized

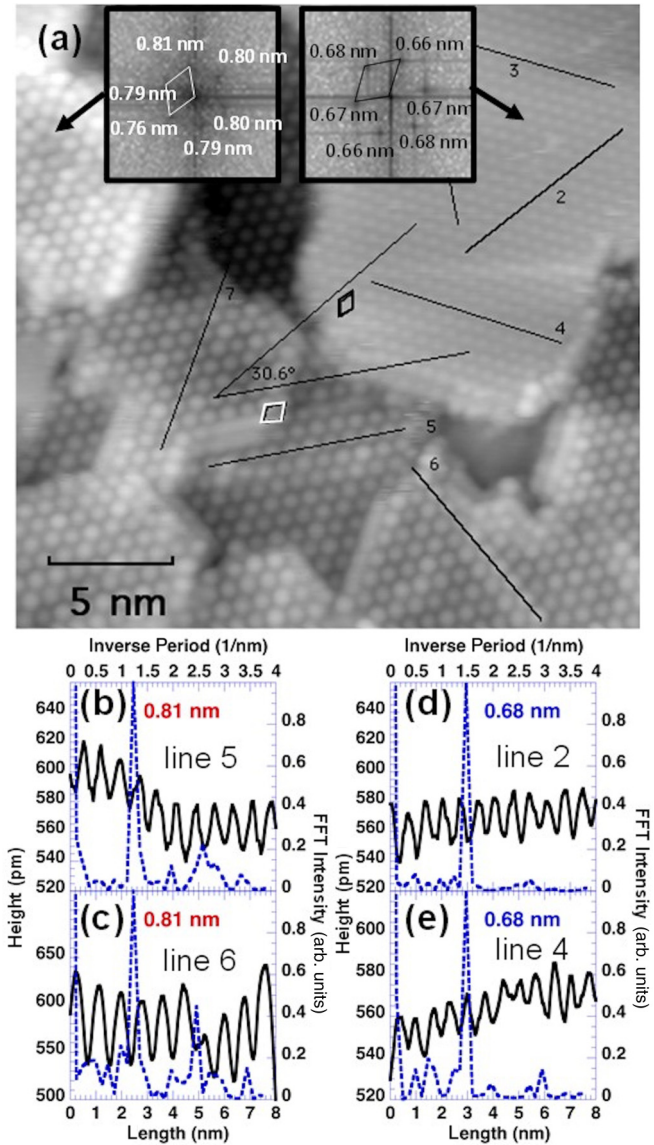


FIG. 6. (a) High-resolution z -image STM of the S4 sample surface [same as the I -mode image in Fig. 5(b)], exemplifying the (b) and (c) (2×2) and (d) and (e) $(\sqrt{3} \times \sqrt{3})R30^\circ$ symmetry and periodicity measurements in a topographic mode, using 2D power spectrum with fast Fourier transform (FFT [top insets in (a)] and 1D FFT power spectrum (blue broken line) of profile plots (black continuous) scanned along randomly chosen black lines in (a) parallel to the three principle (2×2) and $(\sqrt{3} \times \sqrt{3})R30^\circ$ directions. The (2×2) and $(\sqrt{3} \times \sqrt{3})R30^\circ$ unit cells in real and reciprocal space are outlined in white and black in (a) and the insets, respectively, in excellent agreement with the measured rotation angle of 30.6° and respective lattice constants of 0.79 nm and 0.67 nm.

in-plane magnetization curves measured at 4 K. Top left insets in Figs. 7(d)–7(f) magnify the central region of the corresponding magnetization curves at 4 K, whereas the bottom right insets are magnifications of the same central regions of magnetization curves measured at 300 K. Figures 8(a) and 8(b) show magnified STM images of the characteristic silicide island shapes of samples S4 and S5, respectively. Figures 8(c) and 8(d) demonstrate their corresponding normalized in-plane

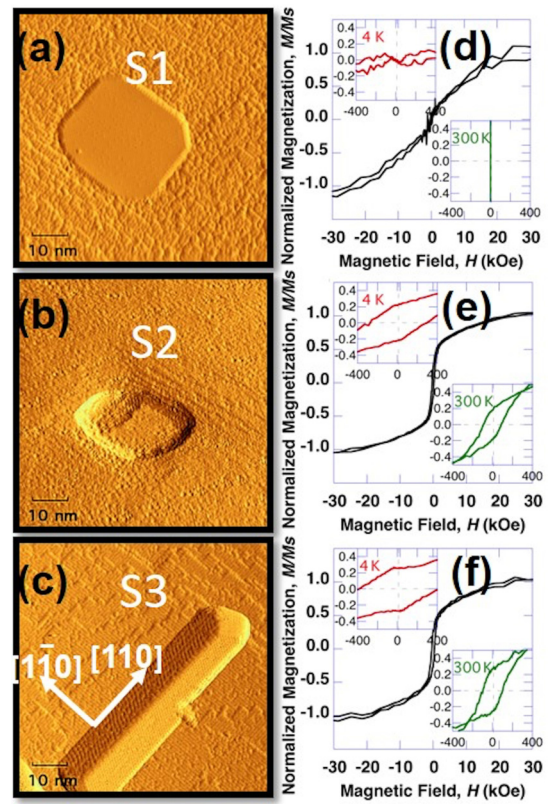


FIG. 7. (d)–(f) In-plane magnetization curves at 4 K, normalized to the saturation magnetic moment, of the (a)–(c) iron-silicide samples S1–S3 (high-resolution I -image STM). Left-top [bottom-right] insets in (d)–(f) are magnified central regions of magnetization curves at 4 K [300 K]. Magnetic field strength in the insets (x axes) is given in Oersted.

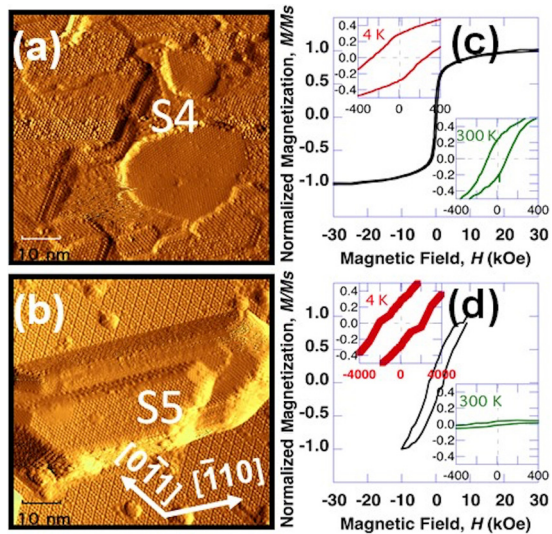


FIG. 8. (c), (d) Normalized to the saturation magnetic moment in-plane magnetization curves at 4 K of the (a) and (b) iron-silicide samples S1 and S3 (high-resolution I -image STM), respectively. Left-top [bottom-right] insets in (c) and (d) are magnified central regions of magnetization curves at 4 K [300 K]. Magnetic field strength in the insets (x axes) is given in Oersted.

magnetization curves at 4 K. Top left insets in Figs. 8(c) and 8(d) magnify the central region of the magnetization curve of samples S4 and S5 at 4 K, whereas the bottom right insets are magnifications of the same central regions at 300 K. Note that the magnetic field strength in Figs. 7(d)–7(f) and 8(c) and 8(d) is given in a k Oersted scale, whereas in the insets the scale is in Oersteds. Sample S1 showed no hysteresis [Figs. 7(a) and 7(d)] and maintained a closed loop even at 4 K [Fig. 7(d)]. Samples S2–S4 exhibit a SPM response, namely an almost entirely closed loop S-shape at RT and a narrow loop opening at 4 K, with 4 K coercivities in the 250 Oe $< H_C <$ 400 Oe range. Sample S5 shows an anomalously wide hysteresis loop at 4 K with coercive field H_C well above 2 kOe [Fig. 8(d)]. Out-of-plane magnetization curves remained closed even at 4 K [40]. For samples S2–S4, no tangible signal was detected with magnetic field applied perpendicular to the sample surface.

IV. DISCUSSION

The results above, and those reported in the literature, point to the fact that silicide phases and metastable structures with stoichiometries considered nonmagnetic in the bulk can show ferromagnetic response at the nanoscale as single-domain nanoparticles. Superparamagnetism occurs for noninteracting single-domain nanoparticles because a single nanoparticle is analogous to a paramagnetic atom with an overall magnetic moment being the sum of moments inside the particle, hence, the higher magnetic susceptibility in comparison with a paramagnet. The simplest approximation of uniaxially anisotropic rotationally symmetric cases is described by the Stoner-Wohlfarth model, where in the absence of external magnetic field, the magnetic orientational potential energy has two degenerate minima with the nanoparticle magnetic moment either parallel or antiparallel to the anisotropy axis [5,11,12,16]. The energy barrier between the two minima is KV , with K reflecting all the magnetic anisotropy contributions and V is the nanoparticle volume. Consequently, at small particle volumes, the energy barrier becomes comparable to the available thermal energy, causing moments to flip between the two minima above the blocking temperature ($T > T_b$) within the duration of the measurement. Therefore, increasing the magnetic anisotropy can overcome the SPM limit by increasing the energy barrier, thus raising the blocking temperature based on the Néel-Arrhenius activation law [5,11,12,16–23].

While in bulk crystals magnetocrystalline anisotropy can be most significant, in small heteroepitaxial deposits, shape, surface, distribution or proximity, and magnetoelastic anisotropies can dominate the MAE [12]. Using epitaxial SA/SO nanostructure growth, some of these contributions can be controlled by a selected combination of substrate and deposition-annealing conditions. However, beforehand, the existence of magnetic moments in nonmagnetic silicides needs to be addressed.

As discussed in the Introduction, magnetic ordering of bulk paramagnetic Si-rich disilicides has been reported, attributed to defects [36,40,41,50–53]. Néel predicted that such defects form at lattice symmetry-breaking sites, thus contributing significantly to MAE [24,84]. In thin films, the most obvious

symmetry-breaking sites are surfaces and interfaces, and in yet lower dimensional SA/SO nanoislands, edges and corners should be accounted for. Rusponi *et al.* reported on this phenomenon [20,54,85] by showing that undercoordinated Co atoms at the perimeter of 2D Co islands on Pt contribute 20 times more magnetic anisotropy than the more highly coordinated Co atoms within the island's interior. Furthermore, they have demonstrated that the magnetic response of a Pt island decorated by a rim of Co atoms was similar to that of pure Co islands of a similar size, proving that the rim atoms are the main contributors to MAE. In that case, the phenomenon was explained by augmented spin-orbit energy due to increased local density of states near the Fermi level and the spin magnetic moment, following $3d$ -electron localization and band narrowing. Strong spin-orbit coupling of the Pt $5d$ states was pointed to as an additional factor for increased MAE.

In this paper, we believe that Fe atoms with reduced coordination at the rims of iron-silicide islands are the major contributors of magnetic moments and anisotropy energy. If so, MAE can be maximized by maximizing the perimeter length and is thus expected to increase with the island rim/area or length/width aspect ratio, namely in elongated islands, with in-plane magnetization axis parallel to the elongation direction due to magnetic shape anisotropy minimization of the stray field energy [84]. Coercivity measured along an easy axis is a relevant parameter to describe the magnetic anisotropy of the nanoislands [22,23,86,87]. We use the coercive field to rank the relative anisotropy of the epitaxial iron-silicide nanoislands. Thus, we arrange the magnetization curves of our samples not according to the substrate orientation, as in Figs. 7 and 8, but rather in the order of growing length-to-width aspect ratio, as shown for measurements at 4 K in Fig. 9. This results in the following ranking: S1→S4→S2→S3→S5, with respective magnified magnetization curves shown in Figs. 9(a)–9(e). Figure 9(f) summarizes the variation of coercivity with the nanoisland length-to-width aspect ratio. It is noteworthy that in sample S5, on the Si(111) substrate, the magnetic field is applied parallel to the long, easy axis of the SO elongated islands, unlike in the Si(001) samples (S1–S3). In these two latter samples, two mutually perpendicular $\langle 110 \rangle$ directions offer energetically degenerate step orientations and island elongation directions, resulting in a mixture of easy and hard axes in roughly equal proportions. Figure 9 highlights the structure-property relations in these iron-silicide nanoislands, namely the effect of the island lateral shape anisotropy on the coercivity. Starting with the most compact S1 islands, which show no coercivity even at 4 K [Fig. 9(a)], the coercivity then increases gradually with the SA island anisotropic elongation [Figs. 9(b)–9(d)], culminating with a steep jump from hundreds of Oersteds to thousands of Oersteds in the most elongated SO islands in Fig. 9(e). The increasing trend in Fig. 9(f) is apparent, though we note large error bars due to a broad scattering of the characteristic shapes of epitaxial SA islands (e.g., STM images shown in Fig. 1, in particular sample S3).

Nanoislands in samples S2–S4 exhibit SPM behavior of small, single-domain, noninteracting nanoparticles, with low coercivity and remanence even at 4 K, and low blocking ($30 \text{ K} < T_b < 50 \text{ K}$) and zero FC (ZFC)/FC splitting temperatures ($70 \text{ K} < T_s < 130 \text{ K}$). As T_b is related to the energy

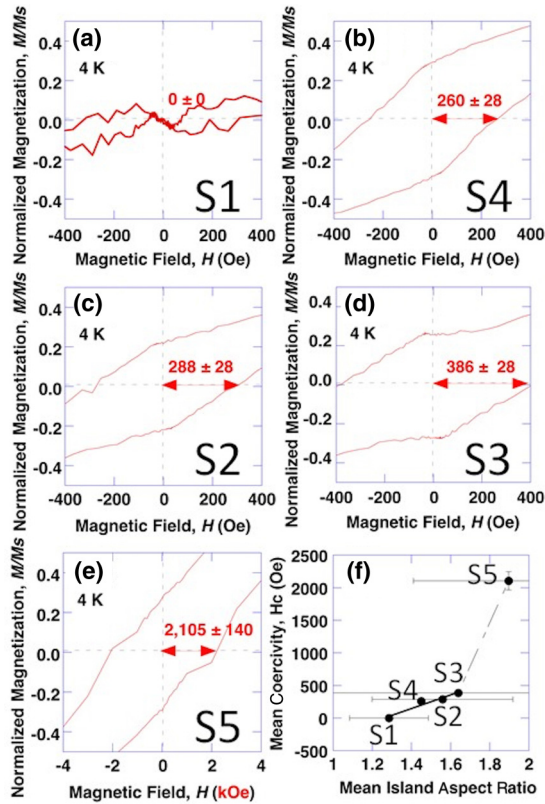


FIG. 9. (a)–(e) Magnified central regions of 4 K magnetization curves of all the samples on Si(001) and Si(111), in the order of increasing magnetic coercivity. Note that the x axis of S5 in (e) is in k Oersteds, whereas the others are in Oersteds. (f) Magnetic coercivity as a function of the mean lateral length/width aspect ratio of the islands. Vertical error bars in (f) indicate the measurement error, and the horizontal bars reflect large scatter of the island shapes.

barrier for magnetization reversal, the difference between T_b and T_s reflects the size-dependent difference between the barriers for variously sized nanoislands in the ensemble due to the broad size distributions in our samples [11]. In other words, T_s corresponds to a maximum blocking temperature, T_B^{\max} , or blocking temperature of the largest nanoparticles, whereas T_b corresponds to an average blocking temperature, T_B^{ave} , of the mean size nanoparticles (or the size distribution center of gravity) [88].

These findings are evident of magnetism in even *a priori* non-MNSs. As explained below, we attribute this magnetic response to differently coordinated edge atoms. The observed SPM behavior is consistent with the limited number of edge atoms in the nanostructures, as well as with the sparse distribution of islands precluding dipolar interactions. Moreover, such a coordination argument may also account for the paramagnetic behavior of the S1 sample, comprised exclusively of compact, isotropically shaped islands. In addition, only these S1 nanoislands have inclined interfaces with the substrate due to faceting [cf. Figs. 1(b) and 4(a)], which may have affected the coordination of the rim atoms, reducing their contribution to MAE.

The S5 nanoislands grew in a SO manner, aligning themselves along the Si(111) step edges [Figs. 1(f) and 1(g)].

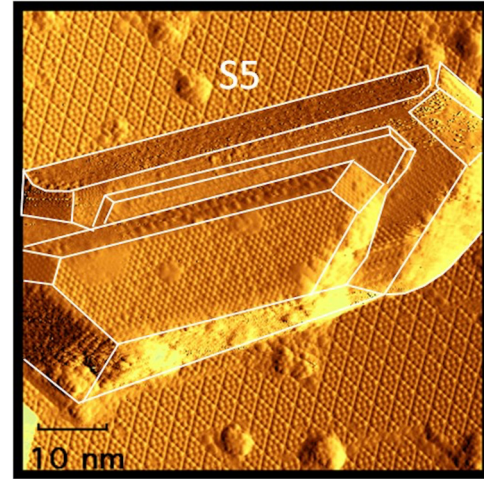


FIG. 10. High-resolution STM I -image of a typical S5 island, with multiple edges outlined in white.

These nanoislands also differ from those of S1–S4 samples in their shape, size, morphology, and geometry [Fig. 8(b)]. Note their unique multi-terrace shape [Fig. 10] observed in all islands [Figs. 1(f) and 1(g)], characterized by a multitude of edges. Thus, the effective perimeter of such islands is considerably longer than in a single-terrace island of the same length-to-width aspect ratio. Furthermore, the proximity of these step edges in the island can enhance internal dipolar interactions in addition to those between islands. In some cases, step edges are observed within atomic scale distances, thus possibly enabling exchange interactions. Therefore, although the α -FeSi₂ structure [40] was not expected to be more magnetic than γ -FeSi₂ in the other samples, the S5 measured magnetic properties pointed to a more collective form of magnetism than in S1–S4. Those collective forms of response are manifested in the shape of magnetization and ZFC/FC curves, blocking and splitting temperatures ($T_b =$

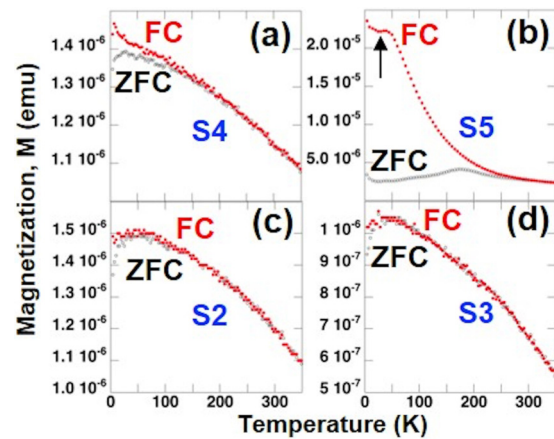


FIG. 11. The ZFC (black open circles)/FC (red filled circles) magnetization curves for comparison of (a) S4 and (b) S5 islands grown on the same Si(111) surface. Note the saturation and the dip (pointed to by an arrow) in the S5 FC curve at low temperatures in (b). Similarly, (c) and (d) show ZFC/FC magnetization curves for the S2 and S3 samples grown on Si(001) substrates.

175 K, $T_s = 320$ K), and coercivity ($H_c > 2$ kOe) more than a fivefold increase compared to the highest of other samples. These relatively high blocking and splitting temperatures can be at least partially accounted for by a marked increase in the number of perimeter atoms. Very close proximity of the islands to one another along the ordering step decoration direction implies chainlike coupling via dipolar interactions. While dipolar interactions are weaker than direct exchange, their collective effect on the magnetic response of the closely spaced nanoislands in S5 may still be significant enough to increase both the coercivity and the critical temperature (akin to T_b in the absence of interactions). Thus, a new magnetic state is introduced, ranging from superspin glass (SSG) to superferromagnetism (SFM; or dipolar ferromagnetism) at stronger interactions [6,11,22,24,89–93]. Saturation of the FC curve at low temperatures, as in sample S5 shown in Fig. 11(b), is evidence of collectiveness due to dipolar island-island interactions. The shallow minimum [arrowed in Fig. 11(b)] instead of plateau is further indicative of a more SSG than SFM character [89,90]. In the absence of interactions, magnetic susceptibility and hence the FC curve slope are expected to follow approximately Curie's $\sim 1/T$ slope. Note that for samples S2–S4, the FC magnetization values at low temperatures are an order of magnitude lower than for sample S5.

V. CONCLUSIONS

We aimed at tuning the magnetic response of epitaxially SA Si-rich silicide nanoisland arrays on Si substrates by systematically varying the nanoisland size, shape, and distribution. The five resulting samples with differently shaped silicide nanoislands exhibited shape-dependent magnetic response, including hysteretic curves in the low-temperature blocked state. We note that none of the samples contained the bulk-ferromagnetic Fe-rich silicide phases. We conclude the

following:

(1) Magnetism of nonferromagnetic phases is attributed to undercoordinated atoms located at the symmetry breaking extremities, such as nanoisland edges. This conclusion follows from the scaling of coercive fields with the island length-to-width aspect ratio, implying a higher contribution of the perimeter atoms to the MAE. As the nanosilicides are of a ferromagnetic transition metal, we assume that Fe rim atoms generate the measured magnetic moments. We are exploring this hypothesis further by experimenting with silicides of nonmagnetic metals [55].

(2) So far, transition to a SPM state with reduction of crystal size to a single domain has been associated with ferro- or ferrimagnetic materials. This paper shows that initial ferro- or ferrimagnetic state need not be a mandatory prerequisite for superparamagnetism as long as there are enough exchange-interacting atoms with magnetic moments at the nanoisland rims.

(3) We demonstrated tuning of the magnetic anisotropy of iron-silicide nanoisland ensembles from paramagnetic zero coercivity through hundreds of Oersteds in the SPM state to thousands of Oersteds, attributed to SSG.

(4) These results can pave the way to using silicides not only as contact materials in microelectronic devices but also as building blocks of high-density storage devices; however, better control over uniformity of SA nanoislands is required. Such control can be achieved using natural (such as periodically stepped surfaces in this research) or lithographically defined templates.

ACKNOWLEDGMENTS

This research was supported by the Israel Science Foundation (Grant No. 1321/13). The authors gratefully acknowledge the valuable technical assistance of M. Levinshtein, L. Burstein, and G. Leitus.

-
- [1] F. X. Redl, K.-S. Cho, C. B. Murray, and S. O'Brien, *Nature* **423**, 968 (2003).
- [2] V. Parekh, E. Chunsheng, D. Smith, A. Ruiz, J. C. Wolfe, P. Ruchhoeft, E. Svedberg, S. Khizroev, and D. Litvinov, *Nanotechnology* **17**, 2079 (2006).
- [3] J. Shin, A. Goyal, C. Cantoni, J. W. Sinclair, and J. R. Thompson, *Nanotechnology* **23**, 155602 (2012).
- [4] B. D. Terris and T. Thomson, *J. Phys. D: Appl. Phys.* **38**, R199 (2005).
- [5] S. A. Majetich, T. Wen, and T. Mefford, *MRS Bull.* **38**, 899 (2013).
- [6] J. I. Martín, J. Nogués, K. Liu, J. L. Vicent, and I. K. Schuller, *J. Magn. Magn. Mater.* **256**, 449 (2003).
- [7] S. Singamaneni, V. N. Bliznyuk, C. Binek, and E. Y. Tsybalc, *J. Mater. Chem.* **21**, 16819 (2011).
- [8] A. Moser, K. Takano, D. T. Margulies, M. Albrecht, Y. Sonobe, Y. Ikeda, S. Sun, and E. E. Fullerton, *J. Phys. D: Appl. Phys.* **35**, R157 (2002).
- [9] J. Mathon and A. Umerski, in *Handbook of Theoretical and Computational Nanotechnology*, edited by M. Rieth and W. Schommers (American Scientific Publishers, Valencia, CA, 2005), Vol. 1, pp. 1–70.
- [10] P. Kervalishvili and A. Lagutin, *Microelectr. J.* **39**, 1060 (2008).
- [11] O. Petravic, *Superlattices Microstruct.* **47**, 569 (2010).
- [12] J. C. Papaefthymiou, *Nano Today* **4**, 438 (2009).
- [13] M. Bode, O. Pietzsch, A. Kubetzka, and R. Wiesendanger, *Phys. Rev. Lett.* **92**, 067201 (2004).
- [14] S. Rohart, P. Campiglio, V. Repain, Y. Nahas, C. Chacon, Y. Girard, J. Lagoute, A. Thiaville, and S. Rousset, *Phys. Rev. Lett.* **104**, 137202 (2010).
- [15] A. Cavallin, F. D. Natterer, S. Ouazi, G. Moulas, A. Lehnert, S. Rusponi, and H. Brune, *Phys. Rev. B* **90**, 144427 (2014).
- [16] F. C. Fonseca, G. F. Goya, R. F. Jardim, R. Muccillo, N. L. V. Carreño, E. Longo, and E. R. Leite, *Phys. Rev. B* **66**, 104406 (2002).
- [17] S. Honda, F. A. Modine, A. Meldrum, J. D. Budai, T. E. Haynes, and L. A. Boatner, *Appl. Phys. Lett.* **77**, 711 (2000).
- [18] X. Xu, B. Lv, F. Wang, X. Li, F. Jiang, and H. Wu, *J. Magn. Magn. Mater.* **310**, 2653 (2007).
- [19] B. D. Cullity, *Introduction to Magnetic Materials* (Addison-Wesley, Reading, MA, 1972).
- [20] S. Ouazi, S. Vlaic, S. Rusponi, G. Moulas, P. Bulushek, K. Halleux, S. Bornemann, S. Mankovsky, J. Minár, J.B. Staunton, H. Ebert, and H. Brune, *Nat. Commun.* **3**, 1313 (2012).

- [21] S. N. Piramanayagam, *J. Appl. Phys.* **102**, 011301 (2007).
- [22] A. Hernado and J. M. González, *Hyperfine Interact.* **130**, 221 (2000).
- [23] H. Kronmüller, *Supermagnets, Hard Magnetic Materials*, edited by G. J. Long and F. Grandjean (Kluwer Academic Publishers, Dordrecht, 1992), p. 461.
- [24] H. Brune, M. Giovannini, K. Bromann, and K. Kern, *Nature* **394**, 451 (1998).
- [25] N. Weiss, T. Cren, M. Epple, S. Rusponi, G. Baudot, S. Rohart, A. Tejada, V. Repain, S. Rousset, P. Ohresser, F. Scheurer, P. Bencok, and H. Brune, *Phys. Rev. Lett.* **95**, 157204 (2005).
- [26] O. Fruchart, *C. R. Physique* **6**, 61 (2005).
- [27] R. Witte, R. Kruk, A. Molinari, D. Wang, S. Schlabach, R. A. Brand, V. Provenzano, and H. Hahn, *J. Phys. D: Appl. Phys.* **50**, 025007 (2017).
- [28] I. Goldfarb and G. A. D. Briggs, *Surf. Sci.* **454–456**, 837 (2000).
- [29] I. Goldfarb and G. A. D. Briggs, *J. Vac. Sci. Technol. B* **20**, 1419 (2002).
- [30] I. Goldfarb, S. Grossman, G. Cohen-Taguri, and M. Levinshtein, *Appl. Surf. Sci.* **238**, 29 (2004).
- [31] I. Goldfarb, S. Grossman, and G. Cohen-Taguri, *Appl. Surf. Sci.* **252**, 5355 (2006).
- [32] I. Goldfarb, *Surf. Sci.* **601**, 2756 (2007).
- [33] I. Goldfarb, E. Roizin, S. Manor, and M. Levinshtein, *Mater. Sci. Semicond. Process.* **12**, 6 (2009).
- [34] I. Goldfarb and G. A. D. Briggs, *Phys. Rev. B* **60**, 4800 (1999).
- [35] I. Goldfarb and G. A. D. Briggs, *J. Mater. Res.* **16**, 744 (2001).
- [36] S. Liang, R. Islam, D. J. Smith, P. A. Bennett, J. R. O'Brien, and B. Taylor, *Appl. Phys. Lett.* **88**, 113111 (2006).
- [37] I. Goldfarb, G. Cohen-Taguri, S. Grossman, and M. Levinshtein, *Phys. Rev. B* **72**, 075430 (2005).
- [38] I. Goldfarb, *Nanotechnology* **18**, 335304 (2007).
- [39] J. K. Tripathi, M. Garbrecht, C. G. Sztrum-Vartash, E. Rabani, W. D. Kaplan, and I. Goldfarb, *Phys. Rev. B* **83**, 165409 (2011).
- [40] J. K. Tripathi, M. Garbrecht, W. D. Kaplan, G. Markovich, and I. Goldfarb, *Nanotechnology* **23**, 495603 (2012).
- [41] J. K. Tripathi, M. Garbrecht, W. D. Kaplan, G. Markovich, and I. Goldfarb, *Appl. Phys. Lett.* **102**, 251604 (2013).
- [42] K. Seo, S. Lee, Y. Jo, M.-H. Jung, J. Kim, D. G. Churchill, and B. Kim, *J. Phys. Chem. C Lett.* **113**, 6902 (2009).
- [43] T. Yoshitake, D. Nakagauchi, and K. Nagayama, *Jpn. J. Appl. Phys.* **42**, L849 (2003).
- [44] W.-L. Chiu, C.-H. Chiu, J.-Y. Chen, C.-W. Huang, Y.-T. Huang, K.-C. Lu, C.-L. Hsin, P.-H. Yeh, and W.-W. Wu, *Nanoscale Res. Lett.* **8**, 290 (2013).
- [45] J.-Y. Lin, H.-M. Hsu, and K.-C. Lu, *Cryst. Eng. Comm.* **17**, 1911 (2015).
- [46] K. Seo, K. S. K. Varadwaj, P. Mohanty, S. Lee, Y. Jo, M.-H. Jung, J. Kim, and B. Kim, *Nano Lett.* **7**, 1240 (2007).
- [47] A. Kawaharazuka, M. Ramsteiner, J. Herfort, H.-P. Schönherr, H. Kostial, and K. H. Ploog, *Appl. Phys. Lett.* **85**, 3492 (2004).
- [48] A. Ionescu, C. A. F. Vaz, T. Trypiniotis, C. M. Gürtler, H. García-Miquel, J. A. C. Bland, M. E. Vickers, R. M. Dalgliesh, S. Langridge, Y. Bugoslavsky, Y. Miyoshi, L. F. Cohen, and K. R. A. Ziebeck, *Phys. Rev. B* **71**, 094401 (2005).
- [49] M.-H. Pan, H. Liu, J.-Z. Wang, J.-F. Jia, Q.-K. Xue, J.-L. Li, S. Qin, U. M. Mirsaidov, X.-R. Wang, J. T. Markert, Z. Zhang, and C.-K. Shih, *Nano Lett.* **5**, 87 (2005).
- [50] Y. Y. Chen, P. C. Lee, C. B. Tsai, S. Neeleshwar, C. R. Wang, J. C. Ho, and H. H. Hamdeh, *Appl. Phys. Lett.* **91**, 251907 (2007).
- [51] H. H. Hamdeh, M. M. Eltabey, J. C. Ho, P. C. Lee, K. Chen, and Y. Y. Chen, *J. Magn. Magn. Mater.* **322**, 2227 (2010).
- [52] G. Cao, D. J. Singh, X.-G. Zhang, G. Samolyuk, L. Qiao, C. Parish, K. Jin, Y. Zhang, H. Guo, S. Tang, W. Wang, J. Yi, C. Cantoni, W. Siemons, E. A. Payzant, M. Biegalski, T. Z. Ward, D. Mandrus, G. M. Stocks, and Z. Gai, *Phys. Rev. Lett.* **114**, 147202 (2015).
- [53] V. S. Zhandun, N. G. Zamkova, S. G. Ovchinnikov, and I. S. Sandalov, *Phys. Rev. B* **95**, 054429 (2017).
- [54] S. Rusponi, T. Cren, N. Weiss, M. Epple, P. Buluschek, L. Claude, and H. Brune, *Nat. Mater.* **2**, 546 (2003).
- [55] J. K. Tripathi, R. Levy, Y. Camus, M. Dascalu, F. Cesura, R. Chalasani, A. Kohn, G. Markovich, and I. Goldfarb, *Appl. Surf. Sci.* **391**, part A, 24 (2017).
- [56] A. Wawro, S. Suto, R. Czajka, and A. Kasuya, *Nanotechnology* **19**, 205706 (2008).
- [57] M. K. Kolel-Veetil and T. M. Keller, *Materials* **3**, 1049 (2003).
- [58] W. Raunau, H. Niehus, and G. Comsa, *Surf. Sci.* **284**, L375 (1993).
- [59] W. Raunau, H. Niehus, T. Schilling, and G. Comsa, *Surf. Sci.* **286**, 203 (1993).
- [60] L. J. Chen, *Mater. Sci. Rep.* **6**, 53 (1991).
- [61] S. S. Lau, J. S.-Y. Feng, J. O. Olowolafe, and M.-A. Nicolet, *Thin Solid Films* **25**, 415 (1975).
- [62] K. Rührnschopf, D. Borgmann, and G. Wedler, *Thin Solid Films* **280**, 171 (1996).
- [63] M. V. Gomoyunova, D. E. Malygin, I. I. Pronin, A. S. Voronchikhin, D. V. Vyalikh, and S. L. Molodtsov, *Surf. Sci.* **601**, 5069 (2007).
- [64] N. Onda, H. Sirringhaus, S. Goncalves-Conto, C. Schwarz, S. Zehnder, and H. von Känel, *Appl. Surf. Sci.* **73**, 124 (1993).
- [65] I. Dézsi, Cs. Fetzter, I. Szűcs, J. Dekoster, A. Vantomme, and M. Caymax, *Surf. Sci.* **599**, 122 (2005).
- [66] S. Walter, F. Blobner, M. Krause, S. Müller, K. Heinz, and U. Starke, *J. Phys.: Condens. Matter* **15**, 5207 (2003).
- [67] K. L. Whiteaker, I. K. Robinson, C. Benson, D. M. Smilgies, N. Onda, and H. von Känel, *Phys. Rev. B* **51**, 9715 (1995).
- [68] H. von Känel, C. Schwarz, S. Goncalves-Conto, E. Müller, L. Miglio, F. Tavazza, and G. Malegori, *Phys. Rev. Lett.* **74**, 1163 (1995).
- [69] U. Starke, J. Schardt, W. Weiss, W. Meier, C. Polop, P. L. de Andres, and K. Heinz, *Europhys. Lett.* **56**, 822 (2001).
- [70] J. Alvarez, J. J. Hinarejos, E. G. Michel, and R. Miranda, *Surf. Sci.* **287–288**, 490 (1993).
- [71] V. L. Thanh, J. Chevrier, and J. Derrien, *Phys. Rev. B* **46**, 15946 (1992).
- [72] H. von Känel, N. Onda, H. Sirringhaus, E. Müller-Gubler, S. Goncalves-Conto, and C. Schwarz, *Appl. Surf. Sci.* **70–71**, 559 (1993).
- [73] J. Chrost, J. J. Hinarejos, P. Segovia, E. G. Michel, and R. Miranda, *Surf. Sci.* **371**, 297 (1997).
- [74] K. Kataoka, K. Hattori, Y. Miyatake, and H. Daimon, *Phys. Rev. B* **74**, 155406 (2006).
- [75] A. N. Hattori, K. Hattori, K. Kataoka, E. Takematsu, A. Ishii, F. Komori, and H. Daimon, *J. Magn. Magn. Mater.* **363**, 158 (2014).

- [76] N. Ohtsu, M. Oku, K. Sato, and K. Wagatsuma, *Appl. Surf. Sci.* **264**, 219 (2013).
- [77] Y. Cao, L. Nyborg, and U. Jelvestam, *Surf. Interface Anal.* **41**, 471 (2009).
- [78] P. L. Tam, Y. Cao, and L. Nyborg, *Surf. Sci.* **606**, 329 (2012).
- [79] B. L. Ong, W. Ong, Y. L. Foo, J. Pan, and E. S. Tok, *Surf. Sci.* **606**, 1649 (2012).
- [80] A. Wawro, S. Suto, R. Czajka, and A. Kasuya, *Phys. Rev. B* **67**, 195401 (2003).
- [81] J. Chevrier, V. Le Thanh, S. Nitsche, and J. Derrien, *Appl. Surf. Sci.* **56–58**, 438 (1992).
- [82] N. Onda, H. Siringhaus, E. Müller, and H. von Känel, *J. Cryst. Growth* **127**, 634 (1993).
- [83] J. J. Hinarejos, P. Segovia, J. Alvarez, G. R. Castro, E. G. Michel, and R. Miranda, *Phys. Rev. B* **57**, 1414 (1998).
- [84] D. Sander, *J. Phys.: Condens. Matter* **16**, R603 (2004).
- [85] P. Gambardella, S. Rusponi, M. Veronese, S. S. Dhesi, C. Grazioli, A. Dallmeyer, I. Cabria, R. Zeller, P. H. Dederichs, K. Kern, C. Carbone, and H. Brune, *Science* **300**, 1130 (2003).
- [86] T. Seki, H. Iwama, T. Shima, and K. Takanashi, *J. Phys. D: Appl. Phys.* **44**, 335001 (2011).
- [87] J. Vértesy and I. Tomáš, *J. Magn. Magn. Mater.* **160**, 25 (1996).
- [88] M. F. Hansen and S. Mørup, *J. Magn. Magn. Mater.* **203**, 214 (1999).
- [89] V. Russier, *J. Magn. Magn. Mater.* **409**, 50 (2016).
- [90] O. Petravic, X. Chen, S. Bedanta, W. Kleemann, S. Sahoo, S. Cardoso, and P. P. Freitas, *J. Magn. Magn. Mater.* **300**, 192 (2006).
- [91] S. Bedanta, O. Petravic, X. Chen, J. Rhensius, S. Bedanta, E. Kentzinger, U. Rücker, T. Brückel, A. Doran, A. Scholl, S. Cardoso, P. P. Freitas, and W. Kleemann, *J. Phys. D: Appl. Phys.* **43**, 474002 (2010).
- [92] S. Bedanta, T. Seki, H. Iwama, T. Shima, and T. Takanashi, *Appl. Phys. Lett.* **107**, 152410 (2015).
- [93] T. Aign, P. Meyer, S. Lemerle, J. P. Jamet, J. Ferré, V. Mathet, C. Chappert, J. Gierak, C. Vieu, F. Rousseaux, H. Launois, and H. Bernas, *Phys. Rev. Lett.* **81**, 5656 (1998).